ANNUAL REVIEWS

Annual Review of Physical Chemistry

Probing the Nature of the Transition-Metal-Boron Bonds and Novel Aromaticity in Small Metal-Doped Boron Clusters Using Photoelectron Spectroscopy

Teng-Teng Chen,[1,2] Ling Fung Cheung,[1,3] and Lai-Sheng Wang[1]

[1]Department of Chemistry, Brown University, Providence, Rhode Island, USA; email: lai-sheng_wang@brown.edu

[2]Department of Chemistry and Biochemistry, University of California San Diego, La Jolla, California, USA

[3]Hitachi Ltd., Research and Development Group, Center for Technology Innovation-Decarbonized Energy, Hitachi-shi, Ibaraki-ken, Japan

Annu. Rev. Phys. Chem. 2022. 73:11.1–11.21

The *Annual Review of Physical Chemistry* is online at physchem.annualreviews.org

https://doi.org/10.1146/annurev-physchem-082820-113041

Keywords

photoelectron spectroscopy, velocity-map imaging, metal-boron chemical bonding, transition-metal boride clusters, boron-metal quadruple bonds, aromaticity

Abstract

Photoelectron spectroscopy combined with quantum chemistry has been a powerful approach to elucidate the structures and bonding of size-selected boron clusters (B_n^-), revealing a prevalent planar world that laid the foundation for borophenes. Investigations of metal-doped boron clusters not only lead to novel structures but also provide important information about the metal-boron bonds that are critical to understanding the properties of boride materials. The current review focuses on recent advances in transition-metal-doped boron clusters, including the discoveries of metal-boron multiple bonds and metal-doped novel aromatic boron clusters. The study of the RhB^- and RhB_2O^- clusters led to the discovery of the first quadruple bond between boron and a transition-metal atom, whereas a metal-boron triple

bond was found in ReB_2O^- and IrB_2O^-. The ReB_4^- cluster was shown to be the first metallaborocycle with Möbius aromaticity, and the planar ReB_6^- cluster was found to exhibit aromaticity analogous to metallabenzenes.

1. INTRODUCTION

Boron is electron deficient and possesses unique chemistry very different from that of its carbon neighbor (1). To compensate for the electron deficiency, bulk boron displays numerous allotropes with complex crystal structures consisting of distinctive polyhedral building blocks, especially the icosahedral B_{12} cage (2–4). In contrast to the bulk three-dimensional building blocks, joint experimental and theoretical investigations over the past two decades have revealed that bare boron clusters prefer two-dimensional (2D) structures (5–10). In particular, photoelectron spectroscopy (PES) combined with quantum calculations has been shown to be a powerful approach to elucidate the structures and chemical bonding of size-selected boron clusters (B_n^-), which have been shown to be planar up to B_{38}^- (**Figure 1**) (11–37). Even though the global minimum of neutral B_{40} was discovered to be an all-boron fullerene (borospherene), the most stable structure of the B_{40}^- anion was found to be planar (30). Recently, the global minima of both B_{41}^- and B_{42}^- were shown to be planar (38), whereas the B_{48}^- cluster was found to have a 2D bilayer structure (39, 40). All planar boron clusters feature localized two-center, two-electron (2c-2*e*) σ bonds on the periphery and multicenter delocalized σ and π bonds over the cluster plane (7, 14, 15, 41–43), which is a direct consequence of the electron deficiency of boron. The delocalized σ and π bonds stabilize the planar structures and give rise to multiple aromaticity and the concept of all-boron analogs of polycyclic aromatic hydrocarbons. Among all the planar boron clusters, the discovery of the planar B_{36} cluster with C_{6v} symmetry and a central hexagonal hole (**Figure 1**) provided the first experimental evidence for the viability of 2D boron nanostructures, named borophenes (26), which consist of a triangular lattice with hexagonal vacancies (44, 45). Subsequently, the B_{35}^- cluster was found to have a similar hexagonal structure but with a double hexagonal vacancy, providing a more flexible structural motif to build borophenes (28). Borophenes have been successfully synthesized on Ag(111) substrates (46, 47), becoming a new class of synthetic 2D materials with novel properties (48–51).

Boron can react with metals to form a variety of interesting boride materials with unique properties and wide industrial applications, ranging from the superconducting MgB_2 and superhard transition-metal borides to lanthanide borides with important magnetic properties and ultrahigh thermal conductivities (52–55). Metal-doped boron clusters have become a new research direction in the study of boron clusters because they provide well-defined molecular systems to elucidate the chemical bonding between boron and metals that is important to understanding the properties of boride materials. Main-group metals interact with boron through *s*/*p* orbitals, resulting in either half-sandwich or substitutional structures (56–72). Transition metals are more versatile in bonding with boron, forming a variety of structures including metal-centered boron rings (73–77), half-sandwich structures (78), metal-centered drums (79–82), and planar structures (80, 83, 84). Inspired by the first electron-precise linear BiB_2O^- species with a Bi≡B triple bond (85), we searched for similar MB_2O^- clusters with transition metals. To our surprise, we found RhB_2O^- possessed a bent structure with an extremely short terminal Rh–B bond and a BO boronyl unit coordinated to the Rh atom. Subsequently, we investigated the diatomic RhB^- molecule without the BO coordination and found that it had an even shorter Rh–B bond. Both experimental and theoretical analyses revealed that the B atom engages in quadruple bonding with Rh in the neutral RhB diatomic species and $RhB(BO^-)$ (86). Recently, we have indeed observed a triple bond

PES: photoelectron spectroscopy

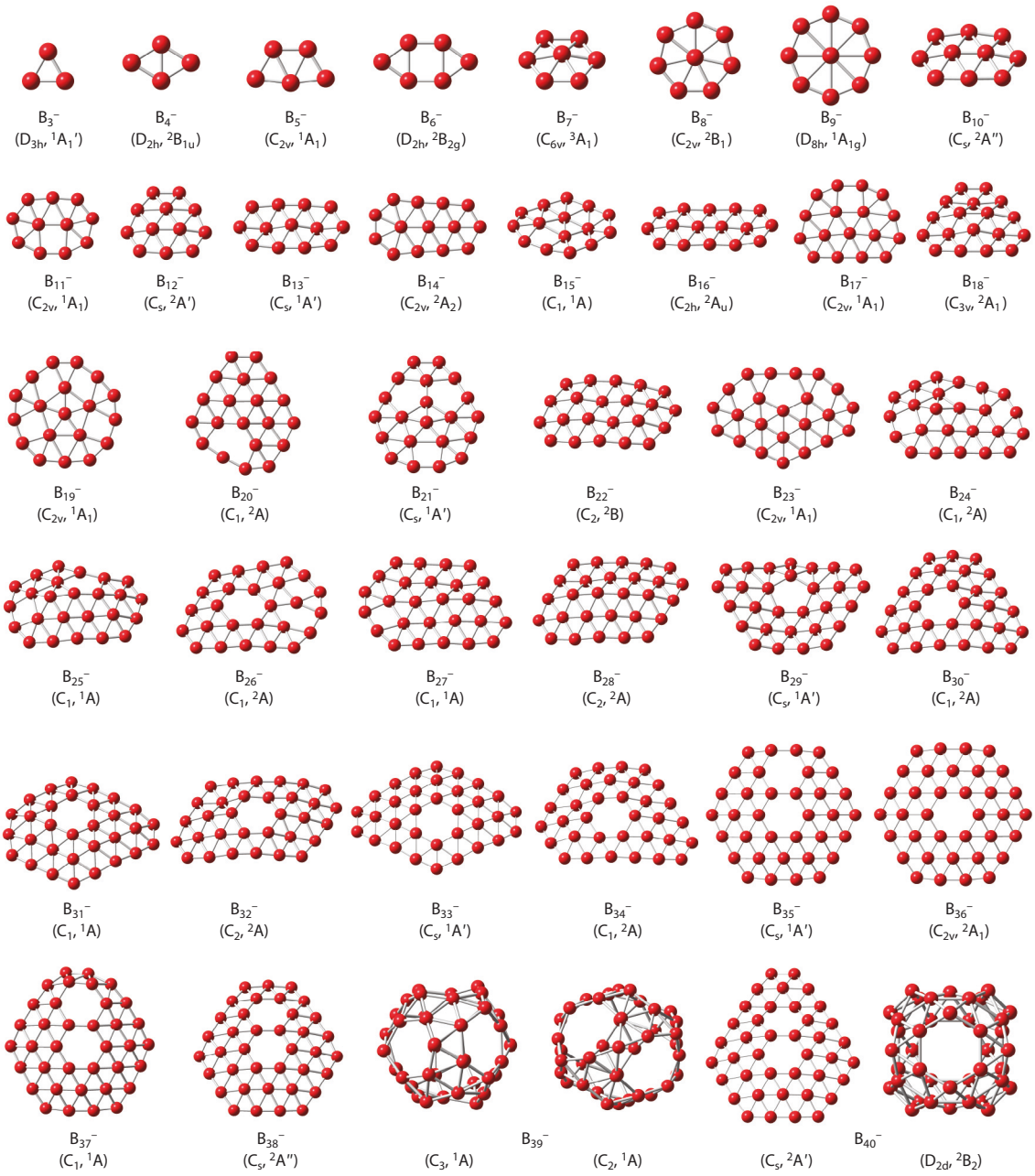

Figure 1

A summary of the global minima of the B_n^- clusters (n = 3–40) confirmed from joint photoelectron spectroscopy and theoretical calculations. The symmetry and electronic state of each cluster are given in the parentheses. Note that a close-lying, three-dimensional isomer is also shown for B_{39}^- and B_{40}^-. Figure adapted with permission from Reference 9.

between boron and a transition metal in ReB_2O^-, the first electron-precise, transition-metal borylyne complex similar to the classical carbyne systems (87). A series of Re-doped boron clusters have been investigated. While ReB_3^- was shown to have a pyramidal structure, the ReB_4^- cluster was found to have a planar pentagonal ring structure (88). Chemical bonding analyses revealed that the pentagonal ReB_4^- was the first simple cyclic Möbius aromatic system. The ReB_6^- cluster was found to be perfectly planar, with a B-centered, six-membered ring with a peripheral Re atom. Chemical bonding analyses showed that ReB_6^- is σ and π doubly aromatic, which can be viewed as a metallaboron analog of metallabenzenes (89). Both ReB_8^- (C_2, ^3A) and ReB_9^- (D_{9h}, $^2A_1'$) were found to possess a central Re atom coordinated by a monocyclic boron ring (90), and both can be considered to be new members of the aromatic borometallic molecular wheel family of metal-doped boron clusters (73–77).

PEI: photoelectron imaging

MO: molecular orbital

KE: kinetic energy

BE: binding energy

VDE: vertical electron detachment energy

ADE: adiabatic electron detachment energy

EA: electron affinity

Several review and perspective articles have been previously published about size-selected and metal-doped boron clusters. Early studies on small boron clusters and their potential as inorganic ligands were reviewed in 2006 (5). Investigations of pure boron clusters using joint PES and theoretical calculations were reviewed extensively in 2016 (8), highlighting the discoveries of borophenes and borospherenes. The chemical bonding and structure fluxionality of boron clusters were discussed in a perspective in 2014 (7) and more recently in 2019 (10). A perspective focusing on the planar CoB_{18}^- and RhB_{18}^- clusters and the viability of metalloborophenes was published in 2017 (84). Very recently, advances in size-selected boron and doped-boron clusters up to 2019 were comprehensively reviewed (9). This review focuses on recent progress in the investigation of transition-metal-doped boron clusters, in particular the discovery of the boron-metal quadruple bonds in RhB and RhB_2O^- (86), the boron-metal triple bond in IrB_2O^- and ReB_2O^- (87), the Möbius aromatic planar metallaborocycle of ReB_4^- (88), and the aromatic ReB_6^- metallaboron analog of metallabenzene (89).

2. PHOTOELECTRON SPECTROSCOPY OF SIZE-SELECTED CLUSTERS

PES is the most powerful experimental technique to investigate the size-dependent electronic properties of size-selected clusters (8, 91, 92). The experimental studies covered in this review were performed using two experimental apparatuses, both equipped with a laser vaporization supersonic cluster source: the first apparatus involves a magnetic-bottle photoelectron analyzer (8, 93) and the second is a high-resolution photoelectron imaging (PEI) system (94, 95). PES directly probes the energy levels of the valence electrons that are responsible for the chemical bonding in nanoclusters. In PES of size-selected clusters, a photon with fixed energy ($h\nu$) emits an electron from the occupied molecular orbitals (MOs) of a negatively charged cluster under the single-particle approximation. By measuring the kinetic energy (KE) of the photoelectron, the binding energy (BE) of the electron in the cluster, $BE = h\nu - KE$, can be obtained. Spectroscopically, the electron-BEs represent the energies for detachment transitions from the ground state of the anion to the ground and excited states of the neutral cluster. The band maximum or the vibrational peak with the largest Franck-Condon factor of a PES band represents the vertical electron detachment energy (VDE), corresponding to a transition from the ground state of the anion to the final state of the underlying neutral at the geometry of the anion. The onset, or the 0–0 transition of the first detachment band, represents the adiabatic electron detachment energy (ADE), which also equals the electron affinity (EA) of the corresponding neutral species. The ADEs and VDEs, as well as vibrational features in favorable cases, provide fingerprints for size-selected clusters and can be used to compare with theoretical calculations to elucidate the structures and bonding of the underlying clusters.

The magnetic-bottle PES apparatus has been described elsewhere (8, 93). Briefly, clusters were produced from a laser vaporization source by focusing the second harmonic of an Nd:YAG laser onto a disk target, which was usually made by cold pressing a mixed powder of isotopically enriched ^{11}B or ^{10}B, the desired dopant metal, and Bi or Ag. The latter was added as a binder in the cold-pressed target and also provided a convenient source of calibrant (Bi^-) in the case of the Bi binder. Negatively charged clusters from the cluster source were analyzed by a time-of-flight (TOF) mass spectrometer, and the clusters of interest were selected by a mass gate before being photodetached by a laser beam. Several detachment energies were used, including the 193-nm (6.424-eV) radiation from an ArF excimer laser and the fourth harmonic (266 nm; 4.661 eV) and third harmonic (355 nm; 3.496 eV) of an Nd:YAG laser. Photoelectrons were collected at almost 100% efficiency by the magnetic bottle and analyzed in a 3.5-m-long electron flight tube. The photoelectron KEs were calibrated using the known spectrum of Bi^-, and the resolution of the apparatus was around 2.5%, i.e., ~25 meV for 1-eV electrons.

The high-resolution PEI apparatus (95) is equipped with a laser vaporization cluster source and a TOF mass spectrometer similar to those of the magnetic-bottle apparatus described above. A key feature of the PEI apparatus is an improved velocity-map imaging (VMI) system that can achieve high-energy resolution over a wider energy range. A Deyang Tech dye laser was used in the PEI experiments. Photoelectrons were focused onto a set of microchannel plates coupled with a phosphor screen and a charge-coupled-device camera. The VMI system was calibrated using Au^- or Bi^- at various photon energies. The typical energy resolution of the VMI system was ~0.6% for high-KE electrons and as low as 1.2 cm^{-1} for very low-energy electrons (95).

TOF: time-of-flight

VMI: velocity-map imaging

3. BORON TRANSITION-METAL MULTIPLE BONDS

Transition metals form a rich class of boride materials with high melting temperatures and high hardness due to the strong boron-metal chemical bonds (96–98). Transition-metal borides have become a new area to search for superhard materials (99) and novel catalysts (100). Clusters of transition-metal borides provide well-defined models to probe the nature of the boron-metal bonds (101, 102), which are essential to understanding the structures and properties of bulk borides. The strong bonding capacities of the *d* orbitals with the boron *s/p* orbitals have led to the observations of a variety of interesting structures and bonding in transition-metal-doped boron clusters. The most surprising finding was the boron-metal quadruple bond in the $RhB(BO^-)$ complex and the diatomic RhB molecule (86). In this section, we discuss this finding and species containing metal-boron triple bonds (87).

3.1. Boron-Metal Quadruple Bonds in RhB and RhB_2O^-

The maximum bond order between two main-group atoms has been known to be three ever since Lewis's (103) epochal work on chemical bonds. However, fourfold bonding has been suggested to exist in diatomic C_2 and similar eight-electron species based on theoretical analyses (104). The quadruple bond in C_2 is controversial, primarily because the putative CC quadruple-bond strength in C_2 is weaker than that in the classical HC≡CH triple bond in terms of bond lengths and force constants (105–108). Boron can form triple bonds with itself (109–111) and with the main-group metal in BiB_2O^-, i.e., $Bi{\equiv}B{-}BO^-$, which is a closed-shell, electron-precise molecule (85). To search for similar triple-bonded $M{\equiv}B{-}BO^-$ molecules with transition metals, we first examined RhB_2O^-. Surprisingly, we found that it did not have the expected linear $Rh{\equiv}B{-}BO^-$ structure. Rather, its most stable structure was found to be bent, with the BO^- ligand coordinated to the Rh atom and a very short terminal Rh–B bond, $RhB(BO^-)$. Subsequently, we investigated the diatomic RhB^- and RhB species and found that they have even shorter Rh–B bonds. Both

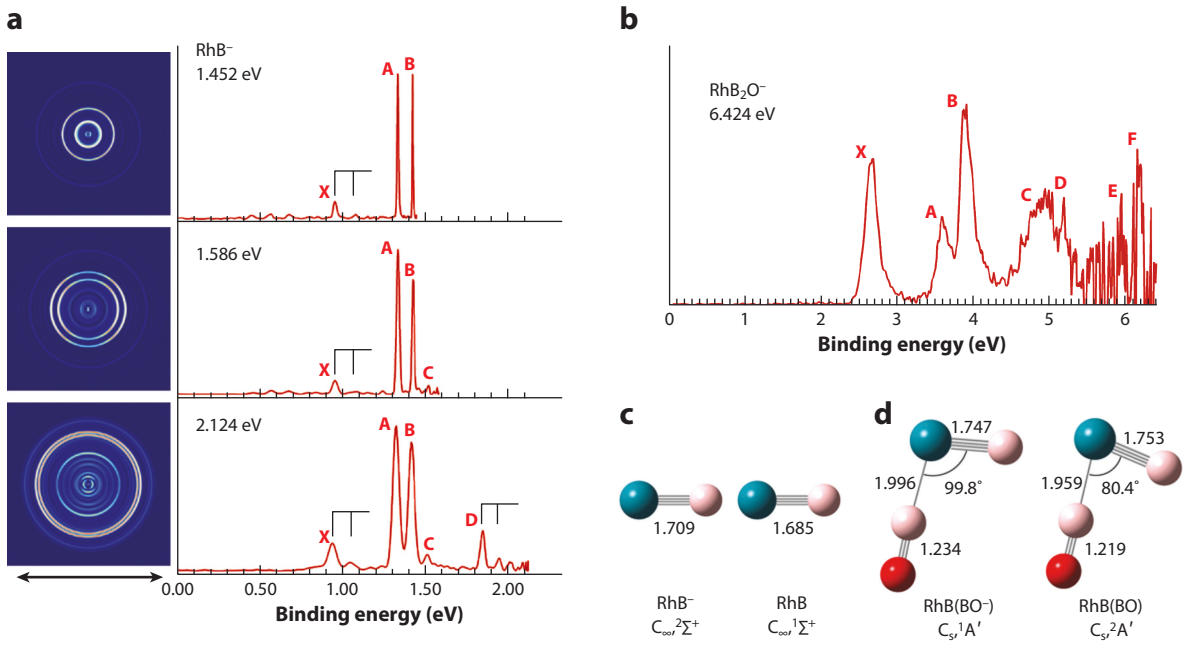

Figure 2

(*a*) Photoelectron images and spectra for RhB^- at three photon energies. (*b*) The photoelectron spectrum of RhB_2O^- at 193 nm (6.424 eV). The photon energies are given in each spectrum, where the letters indicate the resolved photoelectron spectroscopy bands. (*c*) The optimized structures for RhB^- and RhB. (*d*) The optimized structures for $RhB(BO^-)$ and RhB(BO). The symmetry and electronic state are given below each structure. The bond lengths in panels *c* and *d* are given in angstroms. Figure adapted with permission from Reference 86.

experimental and theoretical analyses demonstrated that the B atom engaged in quadruple bonding with Rh in Rh≡B and Rh≡$B(BO^-)$ (86).

Figure 2*a* shows the photoelectron images and spectra of RhB^- at three photon energies using the PEI apparatus. The high-resolution PEI data revealed several electronic states of RhB and the associated vibrational progressions. The photoelectron spectrum of RhB_2O^- shown in **Figure 2*b*** was taken using the magnetic-bottle PES apparatus at 193 nm and displays numerous PES bands. High-resolution PEI data for the ground-state transition gave a broad band with complicated vibrational structures, suggesting large geometry changes between the ground state of RhB_2O^- and that of its neutral. The optimized structures for $RhB^{-/0}$ and $RhB_2O^{-/0}$ are given in **Figure 2*c*** and **2*d***, respectively. The global minimum of RhB_2O^- was found to be bent (C_s, $^1A'$), consisting of a BO^- ligand coordinated to the Rh atom. The calculated Rh–B bond length between Rh and the BO unit was 1.996 Å, while that between Rh and the terminal B was 1.747 Å in the bent global minimum. There was a huge bond angle change between the BO unit and the RhB unit upon electron detachment, reducing from 99.8° in the anion to 80.4° in the neutral. The Rh–BO bond length was also slightly shortened, and that between Rh and the terminal B was slightly lengthened in the neutral. These large geometry changes were consistent with the complicated high-resolution PEI data observed for RhB_2O^-.

The calculated ADEs and VDEs for RhB_2O^- were in good agreement with the PES data, confirming its surprising bent structure, which could be viewed basically as a BO^- ligand coordinated to the RhB unit (**Figure 2*d***). The unusual bent structure of $RhB(BO^-)$ with its short Rh–B bond

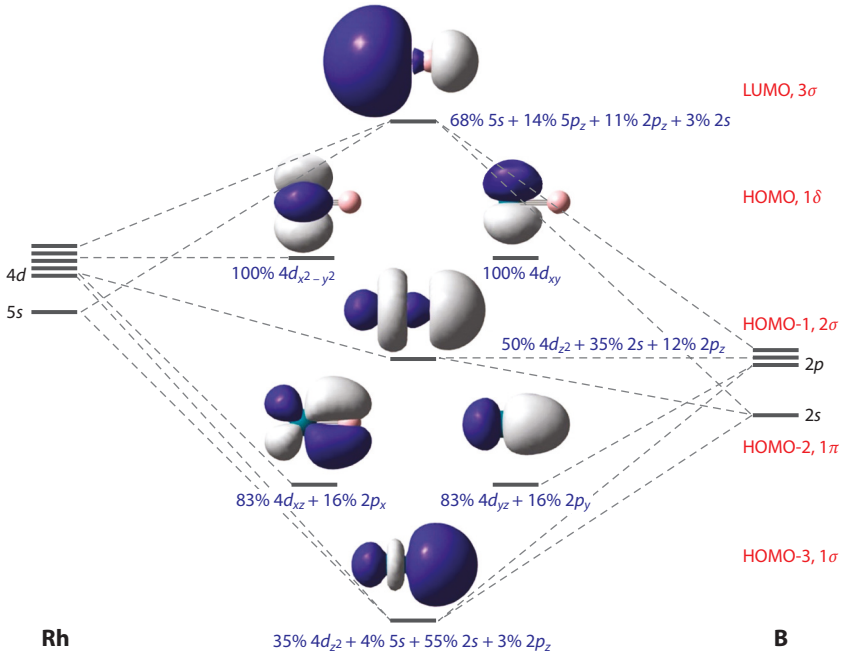

Figure 3

The molecular orbital diagram and compositions for RhB. Abbreviations: HOMO, highest-occupied molecular orbital; LUMO, lowest-unoccupied molecular orbital. Figure adapted with permission from Reference 86.

prompted us to investigate the bonding in the bare RhB diatomic molecule and to conduct the PEI experiment on RhB^-. The computed Rh–B bond length of 1.685 Å was much shorter than the Rh≡B triple bond length (1.79 Å) using Pyykko's self-consistent Rh and B atomic covalent radii (112). Our computed Rh–B bond length agreed well with the previous experimental value of 1.692 Å and the previous theoretical value of 1.698 Å (113, 114). The MOs of RhB (**Figure 3**) revealed four bonding orbitals (1σ, 1π, and 2σ) and two nonbonding orbitals. The extremely short Rh–B bond length was consistent with a quadruple bond between Rh and B. The RhB molecule was previously thought to contain a triple bond because the 1σ MO was classified essentially as a 2*s* lone pair. However, the bonding nature of the 1σ MO can be glimpsed by the fact that the bent Rh≡B(BO^-) structure is more stable than that of the linear Rh≡B–BO^- isomer, in which the B atom can form only a triple bond with Rh (86). The two π MOs in RhB come from bonding interactions between the Rh $4d_{xz}/4d_{yz}$ and the B $2p_x/2p_y$ atomic orbitals, whereas the 2σ MO consists of significant bonding interactions between the Rh $4d_z2$ orbital and the B *sp* hybridized orbital. The lowest-unoccupied MO of RhB, where the extra electron resides in the anion, is weakly antibonding, which is why the bond length of the RhB^- anion is slightly longer than that of RhB.

To further confirm the bonding nature of the 1σ MO in RhB, we investigated the closed-shell $RhBH^+$ species, which can only have an Rh≡B triple bond (**Figure 4*a***). The computed Rh–B bond length was increased from 1.685 to 1.747 Å, whereas the computed Rh–B stretching frequency (**Figure 4*b***) was reduced from 956 cm^{-1} in RhB to 826 cm^{-1} in $RhBH^+$. MO analyses (**Figure 4*c***) clearly showed the Rh≡B triple bond and the single B–H bond in $[Rh{\equiv}B{-}H]^+$. The weakening of the Rh≡B bond in $[Rh{\equiv}B\text{-}H]^+$ relative to that in the bare Rh≡B was consistent with the expectation of the bond order difference. This observation was in contrast to the putative quadruple

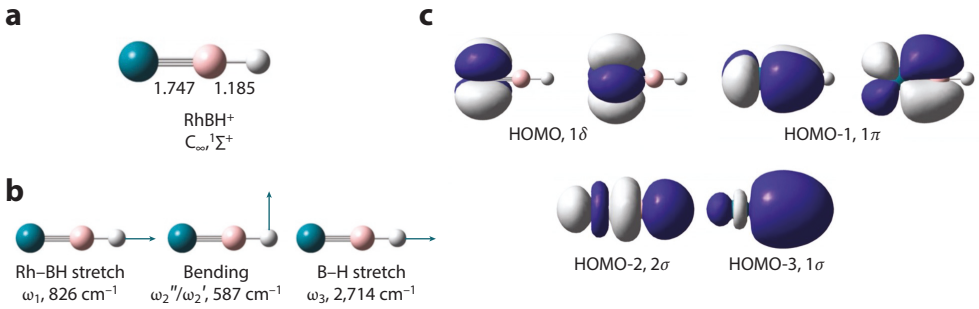

Figure 4

(*a*) The structure, (*b*) vibrational analyses, and (*c*) valence molecular orbitals of $RhBH^+$. The bond lengths in panel *a* are given in angstroms and the symmetry and electronic state are given below the structure. The vibrational modes and their frequencies are given in panel *b*. Abbreviation: HOMO, highest-occupied molecular orbital. Figure adapted with permission from Reference 86.

bond in C_2 (104), which was known to have a longer bond length and smaller vibrational frequency compared to the triple bond in H–C≡C–H (106–108). Thus, there was strong experimental and theoretical evidence that the boron atom engaged in quadruple bonding in the Rh≡B diatomic molecule. In the meantime, an independent study indicated that the boron atom in the $BFe(CO)_3^-$ complex also engaged in quadruple bonding (115), even though the bonding in the diatomic FeB molecule is much weaker (116).

The quadruple bond in Rh≡B is also consistent with the fact that its measured bond dissociation energy is the highest among all the transition-metal diatomic boride molecules (117, 118), even larger than that of the isoelectronic 5*d* IrB. We carried out a subsequent PEI and theoretical study on a series of 5*d* diatomic species, MB^- (M = Ir, Pt, Au), to understand the unique strength of the quadruple bond in Rh≡B (119). The valence MOs of these *M*B species are all similar to that in RhB but with different occupations, as shown in **Figure 5**. The ground state of IrB turned out to be a triplet state ($^3\Delta$) with the promotion of a nonbonding 1δ electron to the 3σ MO. The strong relativistic effects stabilize the 6*s* orbital of Ir (120), resulting in a much smaller energy

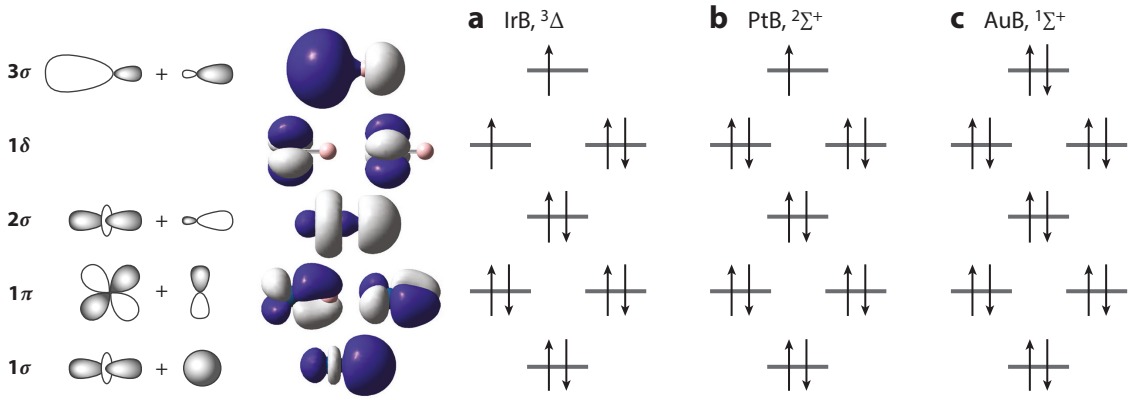

Figure 5

Schematics of the molecular orbital (MO) diagram for (*left*) the transition-metal *M*B (M = Ir, Pt, Au) diatomics and (*right*) the MO occupations for (*a*) IrB, (*b*) PtB, and (*c*) AuB. The electronic state is given for each species. Figure adapted with permission from Reference 119.

separation between the 3σ and 1*δ* MOs in IrB than that in RhB. The occupation of the weakly antibonding 3σ MO weakens the IrB bond relative to that in RhB. The bonding in PtB is similar to that in IrB, whereas the AuB bond is further weakened due to the full occupation of the 3σ MO as well as the weak bonding nature of the 1π MOs. The quadruple bond in RhB has been validated in more sophisticated theoretical analyses (121–123). Tzeli & Karapetsas (122) showed that a quadruple bond also exists in several isoelectronic species, namely TcN, RuC, and PdBe. Schoendorff et al. (123) performed quasi-atomic analyses for the ground and low-lying excited states of RhB. In addition to confirming the quadruple bond in the ground state of RhB, they found that the bond orders become lower in the low-lying excited states due to the promotion of the nonbonding 1*δ* electron to weak antibonding orbitals.

AdNDP: adaptive natural density partitioning

3.2. Boron Transition-Metal Triple Bonds in IrB_2O^- and ReB_2O^-

Multiple bonds between boron and transition metals are known in many borylene (:BR) complexes via B → *M* σ electron donation and metal d_π → BR back donation, despite the electron deficiency of boron (124–126). An electron-precise, metal-boron triple bond was first observed in BiB_2O^- $[Bi{\equiv}B{-}B{\equiv}O]^-$, in which both boron atoms can be viewed as *sp*-hybridized and the $[B{-}BO]^-$ fragment is isoelectronic to a carbyne (85). To search for the first electron-precise, transition-metal-boron, triple-bond species, we investigated IrB_2O^- and ReB_2O^- by PES and quantum chemical calculations (87).

The photoelectron spectra of IrB_2O^- and ReB_2O^- are shown in **Figure *6a*** and ***6b***, respectively, at three different photon energies. Calculations found that the global minimum of IrB_2O^- is a bent structure with a BO^- unit coordinated to the Ir atom, which forms a short Ir−B bond with a terminal B atom, similar to the global minimum of RhB_2O^- discussed in Section 3.1 (**Figure *2d***). However, the global minimum of ReB_2O^- is linear, with a short Re−B bond and a BO^- unit bonded to the B atom. The calculated ADEs and VDEs, as well as the vibrational frequencies, were all in good agreement with the experimental data, confirming the bent IrB_2O^- and the linear ReB_2O^- structures. The interesting linear structure for ReB_2O^- was exactly what we were searching for.

We performed chemical bonding analyses for IrB_2O^- and ReB_2O^- using the adaptive natural density partitioning (AdNDP) method (42), as shown in **Figure 7** for ReB_2O^-. The AdNDP results of IrB_2O^- showed that the Ir−B bonding in the boronyl complex was similar to that of the bare IrB molecule discussed in Section 3.1, and the bond order was more appropriately described as a triple bond (87). The AdNDP analyses for the linear ReB_2O^- (**Figure 7**) revealed an Re≡B triple bond, a B≡O triple bond, a single B−B bond, two unpaired electrons in the $5d_{xy}$ and $5d_{x2\text{-}y2}$ orbitals, a 6*s* lone pair, and an O *sp* lone pair. Thus, the linear ReB_2O^- species can be expressed as an $[Re{\equiv}B{-}B{\equiv}O]^-$ in which both B atoms are *sp*-hybridized, similar to that in carbyne complexes (124–126). The Re≡B bond length of 1.842 Å was in good agreement with the value of 1.83 Å obtained from Pyykkö's (112) triple-bond covalent atomic radii. The ReB_2O^- molecule can be considered to be the first electron-precise, transition-metal borylyne complex. The results suggest the intriguing possibility of synthesizing compounds with electron-precise M≡B triple bonds analogous to classical carbyne systems.

4. AROMATIC TRANSITION-METAL-DOPED BORON CLUSTERS

Electron delocalization in the cluster plane is a major bonding characteristic of 2D boron clusters, giving rise to the concepts of π and σ aromaticity and all-boron analogs of polycyclic aromatic hydrocarbons (7, 14, 15). The Hückel rule developed for monocyclic hydrocarbons was found to be

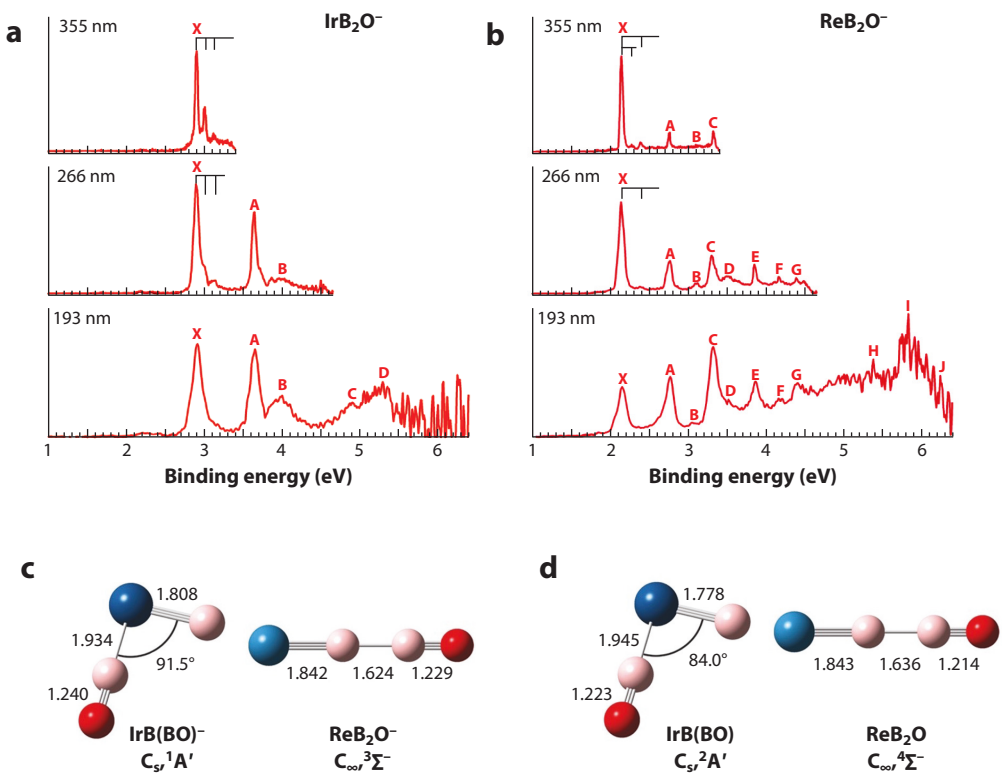

Figure 6

The photoelectron spectra of (*a*) IrB_2O^- and (*b*) ReB_2O^- at three photon energies and the optimized structures for (*c*) the IrB_2O^- and ReB_2O^- anions and (*d*) those of the IrB_2O and ReB_2O neutrals. The detachment laser wavelengths are given in the spectra in panels *a* and *b*, where the letters indicate the resolved photoelectron spectroscopy bands. The symmetry and electronic states are given for each structure in panels *c* and *d*. The bond lengths in panels *c* and *d* are given in angstroms. Figure adapted with permission from Reference 87.

applicable to the planar boron clusters. In fact, transition metals can be doped in the plane of boron clusters due to the strong metal-boron bonding (83, 84). The *d* orbitals of transition metals have been found to participate in the electron delocalization in doped planar boron clusters, resulting in aromatic borometallic clusters, first discovered in the metal-centered molecular wheels, $M©B_n^-$ ($n = 8$–10) (73–77). Recently, it has been discovered that the Re atom can also be positioned on the periphery of small planar boron clusters, resulting in the realization of the first cyclic Möbius aromatic system in ReB_4^- (88) and the metallaboron analog (ReB_6^-) of metallabezenes (89). These recent findings are discussed in this section.

4.1. Möbius Aromaticity in the ReB_4^- Planar Metallaborocycle

A Möbius topology is obtained if one takes a paper strip, twists it by 180°, and then joins its two ends to form a loop. Möbius-type annulenes were found to be aromatic with $4n$ π electrons or antiaromatic with $4n + 2$ π electrons (127, 128). The electron counting rule for Möbius aromaticity is thus opposite to that for Hückel aromaticity, because of the phase change of the overlapping p_z orbitals caused by the 180° twist in the Möbius topology. Interestingly, *d* orbitals can induce a phase change in the overlapping p_z orbitals in planar cyclic systems if the tangential

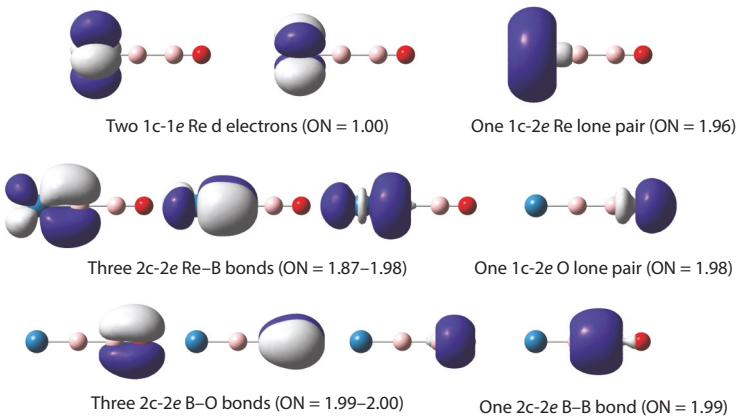

Figure 7

Adaptive natural density partitioning chemical bonding analyses for the linear ReB_2O^- molecule with an ReB triple bond. The c and *e* in the abbreviations stand for center and electron, respectively, while ON stands for occupation number. Figure adapted with permission from Reference 87.

d_π orbital conjugates with the p_z orbitals on the neighboring atoms (129, 130). Planar bicyclic osmapentalynes were synthesized and were shown to exhibit Möbius aromaticity (131). There was significant interest in Möbius aromaticity in planar metallacycles (132, 133), but it was challenging to realize these structures in simple cyclic systems. The first observation of a Möbius aromatic planar metallaborocycle was in the ReB_4^- cluster, which was shown to possess a planar pentagonal structure with 4 π electrons. Its Möbius aromaticity was confirmed by both MO analyses and calculations of magnetic shielding properties (88).

The structure and bonding of ReB_4^- were studied by high-resolution PEI and ab initio calculations. The photoelectron images and spectra of ReB_4^- at four photon energies are shown in **Figure 8*a***. Theoretical calculations showed that the global minimum of ReB_4^- was closed shell with a planar pentagonal ring structure, and the ground state of neutral ReB_4 was a spin-doublet with almost the same structure as that of the anion (**Figure 8*b***). The photoelectron spectra of ReB_4^- showed a strong 0–0 transition with weak vibrational features, consistent with the theoretical result that there was little geometry change between the neutral and the anion. The calculated EA and vibrational frequencies for ReB_4 agreed well with the experimental data, providing strong evidence for the pentagonal ring structure of ReB_4^-.

MO analyses revealed that ReB_4^- contained four π electrons, suggesting an antiaromatic system according to the Hückel rule. Thus, the stability and rigidity of the ring structure for ReB_4^- were unusual. Chemical bonding analyses using the AdNDP method (**Figure 8*c***) revealed two 2c-2*e* Re–B σ bonds and three 2c-2*e* B–B σ bonds around the periphery. In addition, there were two 3c-2*e* σ bonds between two B atoms and Re and two 5c-2*e* delocalized π bonds. Finally, there was one 1c-2*e* Re lone pair, mainly of Re $5d_z2$ character. The presence of the two delocalized π bonds with four π electrons in ReB_4^- did indeed suggest an antiaromatic system according to the $4n + 2$ Hückel rule. However, one of the delocalized π bonds displayed Möbius topology, suggesting that ReB_4^- should be Möbius aromatic according to the $4n$ electron counting rule. The Möbius aromaticity was confirmed by comparing the magnetic shielding properties of the cyclic ReB_4^- with those of benzene. Thus, the pentagonal ReB_4^- cluster was the first planar monocyclic Möbius aromatic system, suggesting there may be more Möbius aromatic metallaboron clusters. Interestingly, the closed shell and cyclic TaB_4^- and TaB_5 clusters, investigated previously (134),

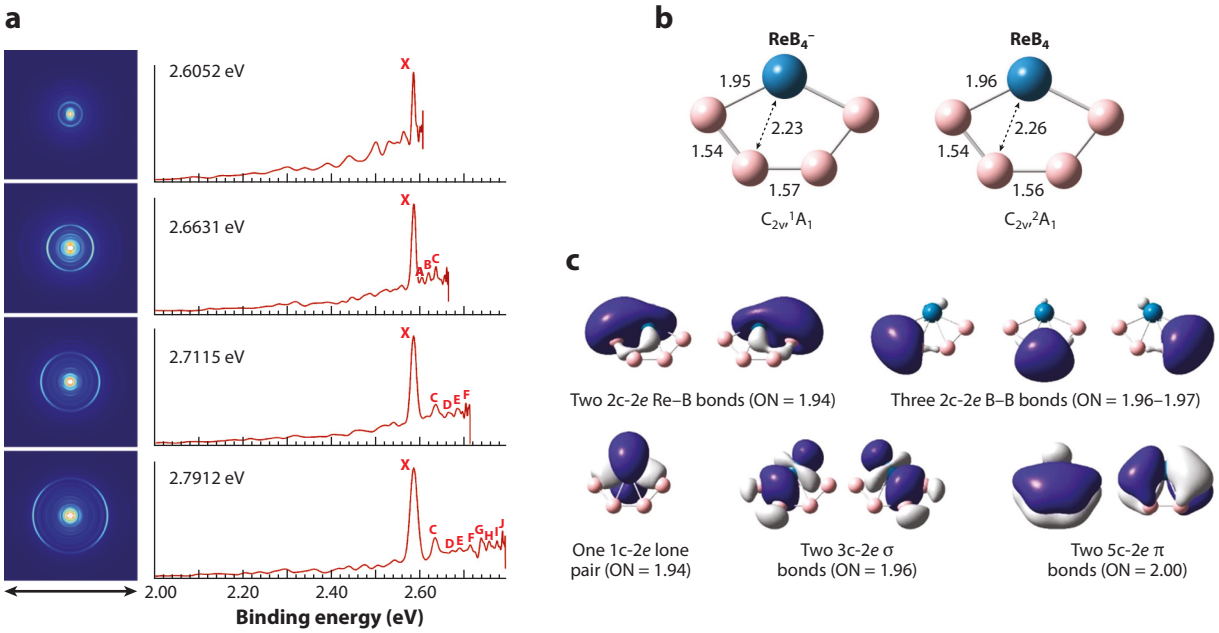

Figure 8

(*a*) Photoelectron images and spectra of ReB_4^- at four photon energies. (*b*) The optimized structures of ReB_4^- and ReB_4; the bond lengths are in angstroms; the symmetry and electronic state are given below each structure. (*c*) Adaptive natural density partitioning chemical bonding analyses for the cyclic ReB_4^- cluster. The c and *e* in the abbreviations stand for center and electron, respectively, while ON stands for occupation number. Figure adapted with permission from Reference 88.

were shown to be Möbius aromatic systems by comparing their bonding and magnetic shielding properties with that of ReB_4^- (88).

4.2. ReB_6^-: A Metallaboron Analog of Metallabenzenes

Metallabenzenes are a class of molecules in which a CH unit in benzene is replaced by a functionalized transition-metal atom (135–137). While all-boron analogs of aromatic and antiaromatic hydrocarbons were well-known, no metallaboron analogs of metallabenzenes were reported. The ReB_6^- cluster was first investigated using a joint PEI and computational study to search for Möbius aromaticity. It was found to possess a planar hexagonal structure with a central B atom and a peripheral Re atom instead of a monocyclic ring structure (89). Chemical bonding analyses showed ReB_6^- to be Hückel aromatic with six π electrons. Its aromaticity was verified by comparison with AlB_6^- (69), which contained four π electrons and was known to have a bent hexagonal structure due to its π antiaromaticity.

The photoelectron images and spectra of ReB_6^- at six different photon energies are shown in **Figure 9*a***. A sharp 0–0 transition (peak X) was observed with very little vibrational excitation, suggesting that ReB_6^- was a highly stable cluster and little geometry change occurred between the anion ground state and that of its corresponding neutral. The global minimum of ReB_6^- was found to be a B-centered, six-membered ring with a peripheral Re atom, perfectly planar with C_{2v} symmetry (**Figure 9*b***). The ReB_6 neutral was found to have the same structure with almost identical structural parameters as those of the anion, in agreement with the sharp photoelectron spectra. To contrast with the observation for ReB_6^-, the AlB_6^- cluster, which was known to have

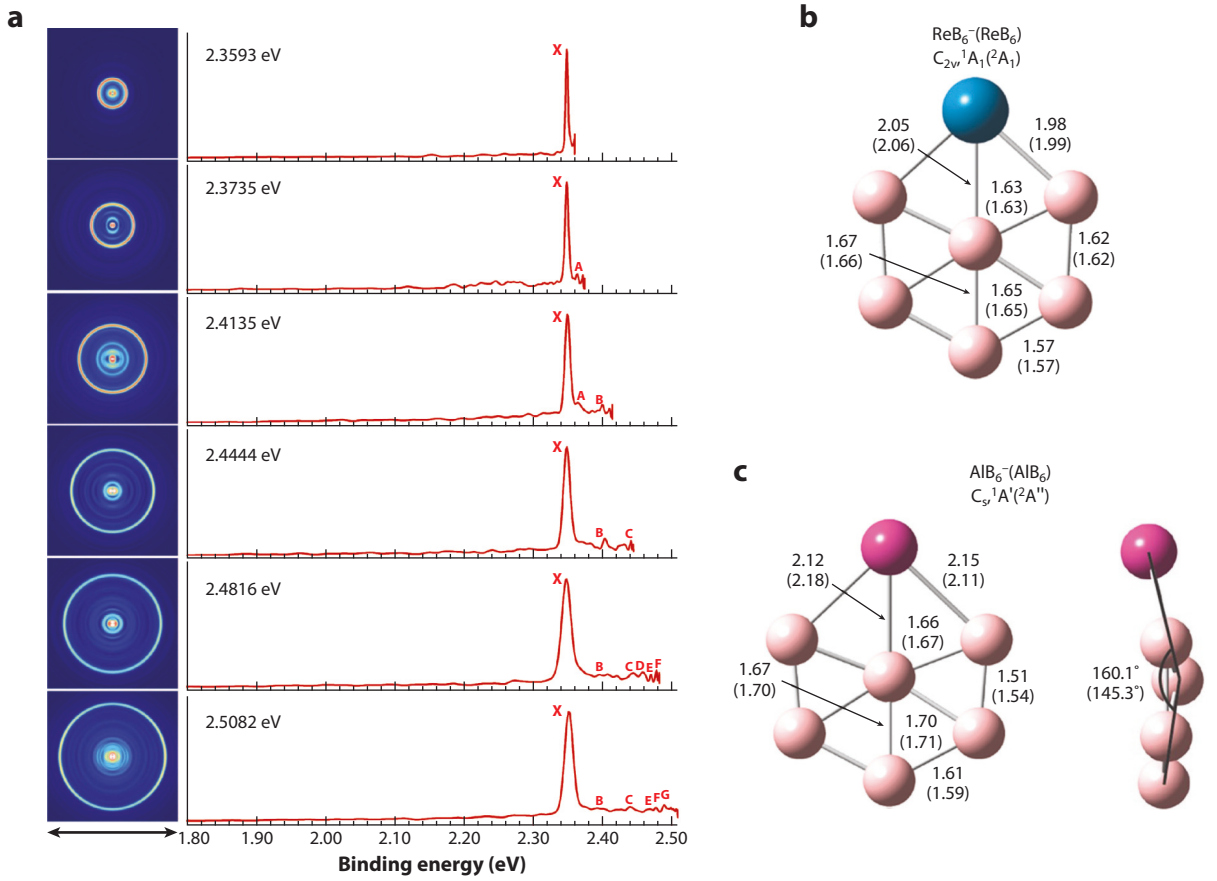

(Caption appears on following page)

Figure 9 (*Figure appears on preceding page*)

(*a*) Photoelectron images and spectra of ReB_6^- at six photon energies. The letters indicate the resolved peaks. (*b*) The optimized structures of ReB_6^- and ReB_6 (in parentheses). (*c*) The optimized structures of AlB_6^- and AlB_6 (in parentheses). The symmetry and electronic states are given below each formula. Bond lengths are given in angstroms and the dihedral angles in $AlB_6^{-/0}$ are in degrees. (*d*) Adaptive natural density partitioning (AdNDP) analyses for the delocalized σ and π bonds in ReB_6^-. (*e*) AdNDP analyses for the delocalized σ and π bonds in AlB_6^-. (*f*) AdNDP analyses for the delocalized π bonds in benzene. (*g*) AdNDP analyses for the delocalized π bonds in $(CO)_4ReC_5H_5$. The c and *e* in the AdNDP results stand for center and electron, respectively, while ON stands for occupation number. Figures adapted with permission from Reference 89.

a similar but nonplanar structure (**Figure 9*c***) (69), was also investigated using high-resolution PEI. Very broad photoelectron spectra were observed with extensive vibrational structures, in agreement with the large bent angle change between the anion and neutral of the AlB_6 cluster.

AdNDP bonding analyses revealed that ReB_6^- is doubly aromatic, with six delocalized σ and six delocalized π electrons (**Figure 9*d***), whereas AlB_6^- is σ aromatic but π antiaromatic with four π electrons (**Figure 9*e***). The delocalized π bonds in ReB_6^- are compared with those in benzene (**Figure 9*f***) and rhenabenzene (**Figure 9*g***) (138). The AlB_6^- cluster provided a rare case of conflicting aromaticity (69). The π antiaromaticity in AlB_6^- explained its out-of-plane distortion, analogous to the out-of-plane distortion of the prototypical antiaromatic cyclooctatetraene (C_8H_8). The three delocalized π bonds in ReB_6^- were found to be similar to those in benzene and rhenabenzene, with the 5*d* orbitals participating in the delocalized bonding. Hence, ReB_6^- can be considered to be a metallaboron analog of metallabenzenes. This finding suggests that other metallaboron analogs of metallabenzenes should exist, and that these species may be viable for bulk syntheses with suitable ligation of the metal site.

5. SUMMARY AND OUTLOOK

PES aided by theoretical calculations has been a powerful technique to elucidate the structures and chemical bonding of nanoclusters. Size-selected boron clusters up to B_{42}^- have been systematically investigated, revealing a structural landscape with prevalent 2D structures as well as all-boron fullerenes (borospherenes). The observation of the planar B_{36} and B_{35} clusters with hexagonal holes provided the first experimental evidence for the viability of 2D borons (borophenes) consisting of a triangular lattice with periodic hexagonal vacancies and laid the foundation for the synthesis of this new class of 2D nanomaterials. Metal doping greatly extends the chemistry of boron clusters, resulting in unprecedented structures and novel chemical bonds. Earlier studies on transition-metal-doped boron clusters have uncovered metal-centered monocyclic rings, half-sandwich structures, metal-centered drums, and metal-imbedded planar structures. Small transition-metal-doped boron clusters with lower boron-to-metal ratios provide significant model systems to probe the chemical bonding between boron and transition metals important in understanding the properties of bulk boride materials. Recent advances in this area are reviewed here. The most exciting finding was the discovery of the Rh≡B quadruple bond in the RhB diatomic and the bent $RhB(BO^-)$ systems. Metal-boron triple bonds were subsequently found in the linear $Re{\equiv}B{-}B{\equiv}O^-$ and bent $Ir{\equiv}B(BO^-)$ clusters. Two Re-doped boron clusters with novel aromaticity are also discussed. The ReB_4^- cluster was found to have a pentagonal ring structure with Möbius aromaticity (four delocalized π electrons), the first planar Möbius aromatic metallaborocycle. The ReB_6^- cluster was found to be perfectly planar, with a B-centered hexagonal structure with double σ and π aromaticity, the first metallaboron analog of metallabenzenes.

The field of size-selected boron clusters is a rich area for scientific inquiries that is still full of surprises and unexpected discoveries. For bare boron clusters, the structures and chemical bonding beyond B_{42}^- are still open. An interesting question is, Will the clusters continue to be planar or cage-like? There are unlimited opportunities for metal-doped boron clusters, though there are

major experimental challenges in terms of mass resolution for arbitrary $M_xB_y^-$ compositions because of the light mass of boron. Clusters of MB_2 stoichiometry are of special interest because many bulk MB_2 borides exhibit superhard properties. Small $(MB_2)_n$ clusters provide model systems to examine the effects of the boron-metal chemical bonding on the properties of the bulk materials. Lanthanides form another important class of boride materials with important magnetic properties. Though not reviewed in the current article, the initial studies on lanthanide boride clusters have revealed very different structures and bonding behaviors from those of transition-metal borides, such as half-sandwich clusters (139), inverse-sandwich clusters (140–143), and the $Ln_3B_{18}^-$ spherical trihedral cage (144). Lanthanide-boride clusters have been relatively less explored (145–150), despite the importance of the bulk lanthanide-boride materials. A detailed understanding of metal-boron bonding will not only allow us to better understand the properties of metal-boride materials but may also lead to the design of novel metal-boron-based materials and new metal-boron compounds. Boron is known as the rule breaker in chemistry due to its electron deficiency that underlies the diversity of structures and bonding observed in bulk boron, boride materials, and boron nanoclusters. We anticipate that boron will continue to produce surprises and unexpected breakthroughs.

DISCLOSURE STATEMENT

The authors are not aware of any affiliations, memberships, funding, or financial holdings that might be perceived as affecting the objectivity of this review.

ACKNOWLEDGMENTS

This research was supported by the National Science Foundation (CHE-2053541). We wish to thank Joseph Czekner, G. Stephen Kocheril, and Wei-Jia Chen for their contributions to the research discussed in this review. The authors are grateful to Alexander Boldyrev and Jun Li for fruitful collaborations and valuable discussions.

LITERATURE CITED

1. Lipscomb WN. 1977. The boranes and their relatives. *Science* 196:1047–55
2. Jemmis ED, Prasad DLVK. 2006. Icosahedral B_{12}, macropolyhedral boranes, β-rhombohedral boron and boron-rich solids. *J. Solid State Chem.* 179:2768–74
3. Albert B, Hillebrecht H. 2009. Boron: elementary challenge for experimenters and theoreticians. *Angew. Chem. Int. Ed.* 48:8640–68
4. Oganov AR, Chen J, Gatti C, Ma YZ, Ma YM, et al. 2009. Ionic high-pressure form of elemental boron. *Nature* 457:863–67
5. Alexandrova AN, Boldyrev AI, Zhai HJ, Wang LS. 2006. All-boron aromatic clusters as potential new inorganic ligands and building blocks in chemistry. *Coord. Chem. Rev.* 250:2811–66
6. Oger E, Crawford NRM, Kelting R, Weis P, Kappes MM, Ahlrichs R. 2007. Boron cluster cations: transition from planar to cylindrical structures. *Angew. Chem. Int. Ed.* 46:8503–6
7. Sergeeva AP, Popov IA, Piazza ZA, Li W-L, Romanescu C, et al. 2014. Understanding boron through size-selected clusters: structure, chemical bonding, and fluxionality. *Acc. Chem. Res.* 47:1349–58
8. Wang L-S. 2016. Photoelectron spectroscopy of size-selected boron clusters: from planar structures to borophenes and borospherenes. *Int. Rev. Phys. Chem.* 35:69–142
9. Jian T, Chen X, Li S-D, Boldyrev AI, Li J, Wang L-S. 2019. Probing the structures and bonding of size-selected boron and doped-boron clusters. *Chem. Soc. Rev.* 48:3550–91
10. Pan S, Barroso J, Jalife S, Heine T, Asmis KR, Merino G. 2019. Fluxional boron clusters: from theory to reality. *Acc. Chem. Res.* 52:2732–44

11. Zhai H-J, Wang L-S, Alexandrova AN, Boldyrev AI. 2002. Electronic structure and chemical bonding of B_5^- and B_5 by photoelectron spectroscopy and *ab initio* calculations. *J. Chem. Phys.* 117:7917–24
12. Alexandrova AN, Boldyrev AI, Zhai H-J, Wang L-S, Steiner E, Fowler PW. 2003. Structure and bonding in B_6^- and B_6: planarity and antiaromaticity. *J. Phys. Chem. A* 107:1359–69
13. Zhai H-J, Wang L-S, Alexandrova AN, Boldyrev AI, Zakrzewski VG. 2003. Photoelectron spectroscopy and ab initio study of B_3^- and B_4^- anions and their neutrals. *J. Phys. Chem. A* 107:9319–28
14. Zhai H-J, Alexandrova AN, Birch KA, Boldyrev AI, Wang L-S. 2003. Hepta- and octacoordinate boron in molecular wheels of eight- and nine-atom boron clusters: observation and confirmation. *Angew. Chem. Int. Ed.* 42:6004–8
15. Zhai H-J, Kiran B, Li J, Wang L-S. 2003. Hydrocarbon analogues of boron clusters—planarity, aromaticity and antiaromaticity. *Nat. Mater.* 2:827–33
16. Alexandrova AN, Boldyrev AI, Zhai H-J, Wang L-S. 2004. Electronic structure, isomerism, and chemical bonding in B_7^- and B_7. *J. Phys. Chem. A* 108:3509–17
17. Kiran B, Bulusu S, Zhai H-J, Yoo S, Zeng XC, Wang L-S. 2005. Planar-to-tubular structural transition in boron clusters: B_{20} as the embryo of single-walled boron nanotubes. *PNAS* 102:961–64
18. Sergeeva AP, Zubarev DY, Zhai H-J, Boldyrev AI, Wang L-S. 2008. A photoelectron spectroscopic and theoretical study of B_{16}^- and B_{16}^{2-}: an all-boron naphthalene. *J. Am. Chem. Soc.* 130:7244–46
19. Pan L-L, Li J, Wang L-S. 2008. Low-lying isomers of the B_9^- boron cluster: the planar molecular wheel versus three-dimensional structures. *J. Chem. Phys.* 129:024302
20. Huang W, Sergeeva AP, Zhai H-J, Averkiev BB, Wang L-S, Boldyrev AI. 2010. A concentric planar doubly π-aromatic B_{19}^- cluster. *Nat. Chem.* 2:202–6
21. Sergeeva AP, Averkiev BB, Zhai H-J, Boldyrev AI, Wang L-S. 2011. All-boron analogues of aromatic hydrocarbons: B_{17}^- and B_{18}^-. *J. Chem. Phys.* 134:224304
22. Li W-L, Romanescu C, Jian T, Wang L-S. 2012. Elongation of planar boron clusters by hydrogenation: boron analogues of polyenes. *J. Am. Chem. Soc.* 134:13228–31
23. Piazza ZA, Li W-L, Romanescu C, Sergeeva AP, Wang L-S, Boldyrev AI. 2012. A photoelectron spectroscopy and *ab initio* study of B_{21}^-: Negatively charged boron clusters continue to be planar at 21. *J. Chem. Phys.* 136:104310
24. Sergeeva AP, Piazza ZA, Romanescu C, Li W-L, Boldyrev AI, Wang L-S. 2012. B_{22}^- and B_{23}^-: all-boron analogues of anthracene and phenanthrene. *J. Am. Chem. Soc.* 134:18065–73
25. Popov IA, Piazza ZA, Li W-L, Wang L-S, Boldyrev AI. 2013. A combined photoelectron spectroscopy and *ab initio* study of the quasi-planar B_{24}^- cluster. *J. Chem. Phys.* 139:144307
26. Piazza ZA, Hu H-S, Li W-L, Zhao Y-F, Li J, Wang L-S. 2014. Planar hexagonal B_{36} as a potential basis for extended single-atom layer boron sheets. *Nat. Commun.* 5:3113
27. Li W-L, Zhao Y-F, Hu H-S, Li J, Wang L-S. 2014. $[B_{30}]^-$: a quasiplanar chiral boron cluster. *Angew. Chem. Int. Ed.* 53:5540–45
28. Li W-L, Chen Q, Tian W-J, Bai H, Zhao Y-F, et al. 2014. The B_{35} cluster with a double-hexagonal vacancy: a new and more flexible structural motif for borophene. *J. Am. Chem. Soc.* 136:12257–60
29. Piazza ZA, Popov IA, Li W-L, Pal R, Zeng XC, et al. 2014. A photoelectron spectroscopy and *ab initio* study of the structures and chemical bonding of the B_{25}^- cluster. *J. Chem. Phys.* 141:034303
30. Zhai H-J, Zhao Y-F, Li W-L, Chen Q, Bai H, et al. 2014. Observation of an all-boron fullerene. *Nat. Chem.* 6:727–31
31. Chen Q, Li W-L, Zhao Y-F, Zhang S-Y, Hu H-S, et al. 2015. Experimental and theoretical evidence of an axially chiral borospherene. *ACS Nano* 9:754–60
32. Li W-L, Pal R, Piazza ZA, Zeng XC, Wang L-S. 2015. B_{27}^-: appearance of the smallest planar boron cluster containing a hexagonal vacancy. *J. Chem. Phys.* 142:204305
33. Wang Y-J, Zhao Y-F, Li W-L, Jian T, Chen Q, et al. 2016. Observation and characterization of the smallest borospherene, B_{28}^- and B_{28}. *J. Chem. Phys.* 144:064307
34. Chen Q, Li W-L, Zhao X-Y, Li H-R, Feng L-Y, et al. 2017. B_{33}^- and B_{34}^-: aromatic planar boron clusters with a hexagonal vacancy. *Eur. J. Inorg. Chem.* 2017:4546–51
35. Chen Q, Tian W-J, Feng L-Y, Lu H-G, Mu Y-W, et al. 2017. Planar B_{38}^- and B_{37}^- clusters with a double-hexagonal vacancy: molecular motifs for borophenes. *Nanoscale* 9:4550–57

36. Luo X-M, Jian T, Cheng L-J, Li W-L, Chen Q, et al. 2017. B_{26}^-: the smallest planar boron cluster with a hexagonal vacancy and a complicated potential landscape. *Chem. Phys. Lett.* 683:336–41
37. Chen Q, Chen T-T, Li H-R, Zhao X-Y, Chen W-J, et al. 2019. B_{31}^- and B_{32}^-: chiral quasi-planar boron clusters. *Nanoscale* 11:9698–704
38. Bai H, Chen T-T, Chen Q, Zhao X-Y, Zhang Y-Y, et al. 2019. Planar B_{41}^- and B_{42}^- clusters with double-hexagonal vacancies. *Nanoscale* 11:23286–95
39. Chen WJ, Ma YY, Chen TT, Ao MZ, Yuan DF, et al. 2021. B_{48}^-: a bilayer boron cluster. *Nanoscale* 13:3868–76
40. Sai L, Wu X, Gao N, Zhao J, King RB. 2017. Boron clusters with 46, 48, and 50 atoms: competition among core-shell, bilayer and quasi-planar structures. *Nanoscale* 9:13905–9
41. Zubarev DY, Boldyrev AI. 2007. Comprehensive analysis of chemical bonding in boron clusters. *J. Comput. Chem.* 28:251–68
42. Zubarev DY, Boldyrev AI. 2008. Developing paradigms of chemical bonding: adaptive natural density partitioning. *Phys. Chem. Chem. Phys.* 10:5207–17
43. Boldyrev AI, Wang L-S. 2016. Beyond organic chemistry: aromaticity in atomic clusters. *Phys. Chem. Chem. Phys.* 18:11589–605
44. Tang H, Ismail-Beigi S. 2007. Novel precursors for boron nanotubes: the competition of two-center and three-center bonding in boron sheets. *Phys. Rev. Lett.* 99:115501
45. Yang X, Ding Y, Ni J. 2008. *Ab initio* prediction of stable boron sheets and boron nanotubes: structure, stability, and electronic properties. *Phys. Rev. B* 77:041402
46. Mannix AJ, Zhou X-F, Kiraly B, Wood JD, Alducin D, et al. 2015. Synthesis of borophenes: anisotropic, two-dimensional boron polymorphs. *Science* 350:1513–16
47. Feng B, Zhang J, Zhong Q, Li W, Li S, et al. 2016. Experimental realization of two-dimensional boron sheets. *Nat. Chem.* 8:563
48. Zhang Z, Penev ES, Yakobson BI. 2017. Two-dimensional boron: structures, properties and applications. *Chem. Soc. Rev.* 46:6746–63
49. Kong L, Wu K, Chen L. 2018. Recent progress on borophene: growth and structures. *Front. Phys.* 13:138105
50. Mannix AJ, Zhang Z, Guisinger NP, Yakobson BI, Hersam MC. 2018. Borophene as a prototype for synthetic 2D materials development. *Nat. Nanotechnol.* 13:444–50
51. Xie S-Y, Wang Y, Li X-B. 2019. Flat boron: a new cousin of graphene. *Adv. Mater.* 31:1900392
52. Nagamatsu J, Nakagawa N, Muranaka T, Zenitani Y, Akimitsu J. 2001. Superconductivity at 39 K in magnesium diboride. *Nature* 410:63–64
53. Chung H-Y, Weinberger MB, Levine JB, Kavner A, Yang J-M, et al. 2007. Synthesis of ultra-incompressible superhard rhenium diboride at ambient pressure. *Science* 316:436–39
54. Scheifers JP, Zhang Y, Fokwa BP. 2017. Boron: enabling exciting metal-rich structures and magnetic properties. *Acc. Chem. Res.* 50:2317–25
55. Tian F, Ren Z. 2019. High thermal conductivity in boron arsenide: from prediction to reality. *Angew. Chem. Int. Ed.* 58:5824–31
56. Alexandrova AN, Zhai H-J, Wang L-S, Boldyrev AI. 2004. Molecular wheel B_8^{2-} as a new inorganic ligand. Photoelectron spectroscopy and ab initio characterization of LiB_8^-. *Inorg. Chem.* 43:3552–54
57. Alexandrova AN, Boldyrev AI, Zhai H-J, Wang L-S. 2005. Photoelectron spectroscopy and *ab initio* study of the doubly antiaromatic B_6^{2-} dianion in the LiB_6^- cluster. *J. Chem. Phys.* 122:054313
58. Wang L-M, Huang W, Averkiev BB, Boldyrev AI, Wang L-S. 2007. CB_7^-: experimental and theoretical evidence against hypercoordinate planar carbon. *Angew. Chem. Int. Ed.* 46:4550–53
59. Averkiev BB, Zubarev DY, Wang L-M, Huang W, Wang L-S, Boldyrev AI. 2008. Carbon avoids hypercoordination in CB_6^-, CB_6^{2-}, and $C_2B_5^-$ planar carbon–boron clusters. *J. Am. Chem. Soc.* 130:9248–50
60. Averkiev BB, Wang L-M, Huang W, Wang L-S, Boldyrev AI. 2009. Experimental and theoretical investigations of CB_8^-: towards rational design of hypercoordinated planar chemical species. *Phys. Chem. Chem. Phys.* 11:9840–49
61. Galeev TR, Li W-L, Romanescu C, Černušák I, Wang L-S, Boldyrev AI. 2012. Photoelectron spectroscopy and *ab initio* study of boron-carbon mixed clusters: CB_9^- and $C_2B_8^-$. *J. Chem. Phys.* 137:234306

62. Bai H, Zhai H-J, Li S-D, Wang L-S. 2013. Photoelectron spectroscopy of aromatic compound clusters of the B_{12} all-boron benzene: $B_{12}Au^-$ and $B_{12}(BO)^-$. *Phys. Chem. Chem. Phys.* 15:9646–53
63. Chen Q, Bai H, Zhai H-J, Li S-D, Wang L-S. 2013. Photoelectron spectroscopy of boron-gold alloy clusters and boron boronyl clusters: $B_3Au_n^-$ and $B_3(BO)_n^-$ ($n = 1, 2$). *J. Chem. Phys.* 139:044308
64. Zhai H-J, Chen Q, Bai H, Lu H-G, Li W-L, et al. 2013. Pi and sigma double conjugations in boronyl polyboroene nanoribbons: $B_n(BO)_2^-$ and $B_n(BO)_2$ ($n = 5–12$). *J. Chem. Phys.* 139:174301
65. Tian W-J, Chen W-J, Yan M, Li R, Wei Z-H, et al. 2021. Transition-metal-like bonding behaviors of a boron atom in a boron cluster boronyl complex $[(\eta^7\text{-}B_7)\text{-}B\text{-}BO]^-$. *Chem. Sci.* 12:8157–64
66. Chen W-J, Kulichenko M, Choi HW, Cavanagh J, Yuan D-F, et al. 2021. Photoelectron spectroscopy of size-selected bismuth-boron clusters: BiB_n^- ($n = 6–8$). *J. Phys. Chem. A* 125:6751–60
67. Wang L-M, Averkiev BB, Ramilowski JA, Huang W, Wang L-S, Boldyrev AI. 2010. Planar to linear structural transition in small boron-carbon mixed clusters: $C_xB_{5-x}^-$ ($x = 1–5$). *J. Am. Chem. Soc.* 132:14104–12
68. Galeev TR, Ivanov AS, Romanescu C, Li W-L, Bozhenko KV, Wang L-S, Boldyrev AI. 2011. Molecular wheel to monocyclic ring transition in boron-carbon mixed clusters $C_2B_6^-$ and $C_3B_5^-$. *Phys. Chem. Chem. Phys.* 13:8805–10
69. Romanescu C, Sergeeva AP, Li W-L, Boldyrev AI, Wang L-S. 2011. Planarization of B_7^- and B_{12}^- clusters by isoelectronic substitution: AlB_6^- and AlB_{11}^-. *J. Am. Chem. Soc.* 133:8646–53
70. Galeev TR, Romanescu C, Li W-L, Wang L-S, Boldyrev AI. 2011. Valence isoelectronic substitution in the B_8^- and B_9^- molecular wheels by an Al dopant atom: umbrella-like structures of AlB_7^- and AlB_8^-. *J. Chem. Phys.* 135:104301
71. Li W-L, Romanescu C, Galeev TR, Wang L-S, Boldyrev AI. 2011. Aluminum avoids the central position in AlB_9^- and AlB_{10}^-: photoelectron spectroscopy and ab initio study. *J. Phys. Chem. A* 115:10391–97
72. Cheung LF, Czekner J, Kocheril GS, Wang L-S. 2019. High resolution photoelectron imaging of boron-bismuth binary clusters: $Bi_2B_n^-$ ($n = 2–4$). *J. Chem. Phys.* 150:064304
73. Romanescu C, Galeev TR, Li W-L, Boldyrev AI, Wang L-S. 2011. Aromatic metal-centered monocyclic boron rings: $Co©B_8^-$ and $Ru©B_9^-$. *Angew. Chem. Int. Ed.* 50:9334–37
74. Li W-L, Romanescu C, Galeev TR, Piazza ZA, Boldyrev AI, Wang L-S. 2012. Transition-metal-centered nine-membered boron rings: $M©B_9$ and $M©B_9^-$ (M = Rh, Ir). *J. Am. Chem. Soc.* 134:165–68
75. Galeev TR, Romanescu C, Li W-L, Wang L-S, Boldyrev AI. 2012. Observation of the highest coordination number in planar species: decacoordinated $Ta©B_{10}^-$ and $Nb©B_{10}^-$ anions. *Angew. Chem. Int. Ed.* 51:2101–5
76. Romanescu C, Galeev TR, Sergeeva AP, Li W-L, Wang L-S, Boldyrev AI. 2012. Experimental and computational evidence of octa- and nona-coordinated planar iron-doped boron clusters: $Fe©B_8^-$ and $Fe©B_9^-$. *J. Organomet. Chem.* 721:148–54
77. Romanescu C, Galeev TR, Li W-L, Boldyrev AI, Wang L-S. 2013. Transition-metal-centered monocyclic boron wheel clusters ($M©B_n$): a new class of aromatic borometallic compounds. *Acc. Chem. Res.* 46:350–58
78. Popov IA, Li W-L, Piazza ZA, Boldyrev AI, Wang L-S. 2014. Complexes between planar boron clusters and transition metals: a photoelectron spectroscopy and ab initio study of CoB_{12}^- and RhB_{12}^-. *J. Phys. Chem. A* 118:8098–105
79. Popov IA, Jian T, Lopez GV, Boldyrev AI, Wang L-S. 2015. Cobalt-centred boron molecular drums with the highest coordination number in the CoB_{16}^- cluster. *Nat. Commun.* 6:8654
80. Jian T, Li W-L, Chen X, Chen T-T, Lopez GV, et al. 2016. Competition between drum and quasi-planar structures in RhB_{18}^-: motifs for metallo-boronanotubes and metallo-borophenes. *Chem. Sci.* 7:7020–27
81. Jian T, Li W-L, Popov IA, Lopez GV, Chen X, et al. 2016. Manganese-centered tubular boron cluster–MnB_{16}^-: a new class of transition-metal molecules. *J. Chem. Phys.* 144:154310
82. Li W-L, Jian T, Chen X, Li H-R, Chen T-T, et al. 2017. Observation of a metal-centered B_2-$Ta@B_{18}^-$ tubular molecular rotor and a perfect $Ta@B_{20}^-$ boron drum with the record coordination number of twenty. *Chem. Commun.* 53:1587–90
83. Li W-L, Jian T, Chen X, Chen T-T, Lopez GV, et al. 2016. The planar CoB_{18}^- cluster as a motif for metallo-borophenes. *Angew. Chem. Int. Ed.* 55:7358–63

84. Li W-L, Chen X, Jian T, Chen T-T, Li J, Wang L-S. 2017. From planar boron clusters to borophenes and metalloborophenes. *Nat. Rev. Chem.* 1:71
85. Jian T, Cheung LF, Chen T-T, Wang L-S. 2017. Bismuth–boron multiple bonding in BiB_2O^- and Bi_2B^-. *Angew. Chem. Int. Ed.* 56:9551–55
86. Cheung LF, Chen T-T, Kocheril GS, Chen W-J, Czekner J, Wang L-S. 2020. Observation of four-fold boron–metal bonds in $RhB(BO^-)$ and RhB. *J. Phys. Chem. Lett.* 11:659–63
87. Chen T-T, Cheung LF, Chen W-J, Cavanagh J, Wang L-S. 2020. Observation of transition-metal–boron triple bonds in IrB_2O^- and ReB_2O^-. *Angew. Chem. Int. Ed.* 59:15260–65
88. Cheung LF, Kocheril GS, Czekner J, Wang L-S. 2020. Observation of Möbius aromatic planar metallaborocycles. *J. Am. Chem. Soc.* 142:3356–60
89. Cheung LF, Czekner J, Kocheril GS, Wang L-S. 2019. ReB_6^-: a metallaboron analog of metallabenzenes. *J. Am. Chem. Soc.* 141:17854–60
90. Chen T-T, Li W-L, Bai H, Chen W-J, Dong X-R, et al. 2019. $Re©B_8^-$ and $Re©B_9^-$: new members of the transition-metal-centered borometallic molecular wheel family. *J. Phys. Chem. A* 123:5317–24
91. Weichman ML, Neumark DM. 2018. Slow photoelectron velocity-map imaging of cryogenically cooled anions. *Annu. Rev. Phys. Chem.* 69:101–24
92. Mason JL, Folluo CN, Jarrold CC. 2021. More than little fragments of matter: electronic and molecular structures of clusters. *J. Comput. Chem.* 154:200901
93. Wang L-S, Cheng HS, Fan J. 1995. Photoelectron spectroscopy of size-selected transition metal clusters: Fe_n^-, $n = 3$–24. *J. Chem. Phys.* 102:9480–93
94. Leon I, Yang Z, Wang L-S. 2013. High resolution photoelectron imaging of Au_2^-. *J. Chem. Phys.* 138:184304
95. León I, Yang Z, Liu H-T, Wang L-S. 2014. The design and construction of a high-resolution velocity-map imaging apparatus for photoelectron spectroscopy studies of size-selected clusters. *Rev. Sci. Instrum.* 85:083106
96. Fokwa BP. 2010. Transition-metal-rich borides–fascinating crystal structures and magnetic properties. *Eur. J. Inorg. Chem.* 2010:3075–92
97. Gu Q, Krauss G, Steurer W. 2008. Transition metal borides: superhard versus ultra-incompressible. *Adv. Mater.* 20:3620–26
98. Levine JB, Tolbert SH, Kaner RB. 2009. Advancements in the search for superhard ultra-incompressible metal borides. *Adv. Funct. Mater.* 19:3519–33
99. Kvashnin AG, Allahyari Z, Oganov AR. 2019. Computational discovery of hard and superhard materials. *J. Appl. Phys.* 126:040901
100. Lee E, Park H, Joo H, Fokwa BPT. 2020. Unexpected correlation between boron chain condensation and hydrogen evolution reaction (HER) activity in highly active vanadium borides: enabling predictions. *Angew. Chem. Int. Ed.* 59:11774–78
101. Robinson PJ, Liu G, Ciborowski S, Martinez-Martinez C, Chamorro JR, et al. 2017. Mystery of three borides: differential metal-boron bonding governing superhard structures. *Chem. Mater.* 29:9892–96
102. Sheifers JP, Nguyen RDT, Zhang Y, Fokwa BPT. 2020. Direct correlation of mechanical hardness and chemical bonding in intermetallic double peroskite borides $Sc_2Ir_{6-x}Pd_xB$. *J. Phys. Chem. A* 124:26062–67
103. Lewis GN. 1916. The atom and the molecule. *J. Am. Chem. Soc.* 38:762–85
104. Shaik S, Danovich D, Wu W, Su P, Rzepa HS, Hiberty PC. 2012. Quadruple bonding in C_2 and analogous eight-valence electron species. *Nat. Chem.* 4:195
105. Danovich D, Hiberty PC, Wu W, Rzepa HS, Shaik S. 2014. The nature of the fourth bond in the ground state of C_2: the quadruple bond conundrum. *Chem. Eur. J.* 20:6220–32
106. Xu LT, Dunning TH Jr. 2014. Insights into the perplexing nature of the bonding in C_2 from generalized valence bond calculations. *J. Chem. Theory Comput.* 10:195–201
107. de Sousa DWO, Nascimento MAC. 2016. Is there a quadruple bond in C_2? *J. Chem. Theory Comput.* 12:2234–41
108. Hermann M, Frenking G. 2016. The chemical bond in C_2. *Chem. Eur. J.* 22:4100–8
109. Zhou M, Tsumori N, Li Z, Fan K, Andrews L, Xu Q. 2002. OCBBCO: a neutral molecule with some boron−boron triple bond character. *J. Am. Chem. Soc.* 124:12936–37

110. Li S-D, Zhai H-J, Wang L-S. 2008. $B_2(BO)_2^{2-}$ – diboronyl diborene: a linear molecule with a triple boron−boron bond. *J. Am. Chem. Soc.* 130:2573–79
111. Braunschweig H, Dewhurst RD, Hammond K, Mies J, Radacki K, Vargas A. 2012. Ambient-temperature isolation of a compound with a boron-boron triple bond. *Science* 336:1420–22
112. Pyykkö P. 2015. Additive covalent radii for single-, double-, and triple-bonded molecules and tetrahedrally bonded crystals: a summary. *J. Phys. Chem. A* 119:2326–37
113. Chowdhury P, Balfour W. 2007. A spectroscopic study of the rhodium monoboride molecule. *Mol. Phys.* 105:1619–24
114. Borin AC, Gobbo JP. 2008. Low-lying singlet and triplet electronic states of RhB. *J. Phys. Chem. A* 112:4394–98
115. Chi C, Wang J-Q, Hu H-S, Zhang Y-Y, Li W-L, et al. 2019. Quadruple bonding between iron and boron in the $BFe(CO)_3^-$ complex. *Nat. Commun.* 10:4713
116. Tzeli D, Mavridis A. 2008. Electronic structure and bonding of the 3*d* transition metal borides, MB, M = Sc, Ti, V, Cr, Mn, Fe, Co, Ni, and Cu through all electron *ab initio* calculations. *J. Chem. Phys.* 128:034309
117. Merriles DM, Tieu E, Morse MD. 2019. Bond dissociation energies of FeB, CoB, NiB, RuB, RhB, OsB, IrB, and PtB. *J. Chem. Phys.* 151:044302
118. Merriles DM, Nielson C, Tieu E, Morse MD. 2021. Chemical bonding and electronic structure of the early transition metal borides: ScB, TiB, VB, YB, ZrB, NbB, LaB, HfB, TaB, and WB. *J. Phys. Chem. A* 125:4420–34
119. Cheung LF, Kocheril GS, Czekner J, Wang L-S. 2020. The nature of the chemical bonding in 5d transition-metal diatomic borides MB (M = Ir, Pt, Au). *J. Chem. Phys.* 152:174301
120. Pyykko P. 1988. Relativistic effects in structural chemistry. *Chem. Rev.* 88:563–94
121. Pan S, Manoj S, Frenking G. 2020. Quadruple bonding of bare group-13 atoms in transition metal complexes. *Dalton Trans.* 49:14815–25
122. Tzeli D, Karapetsas I. 2020. Quadruple bonding in the ground and low-lying excited states of the diatomic molecules TcN, RuC, RhB, and PdBe. *J. Phys. Chem. A* 124:6667–81
123. Schoendorff G, Ruedenberg K, Gordon MS. 2021. Multiple bonding in rhodium monoboride. Quasiatomic analyses of the ground and low-lying excited states. *J. Phys. Chem. A* 125:4836–46
124. Vidovic D, Pierce GA, Aldridge S. 2009. Transition metal borylene complexes: boron analogues of classical organometallic systems. *Chem. Commun.* 10:1157–71
125. Braunschweig H, Dewhurst RD, Schneider A. 2010. Electron-precise coordination modes of boron-centered ligands. *Chem. Rev.* 110:3924–57
126. Soleilhavoup M, Bertrand G. 2017. Borylenes: an emerging class of compounds. *Angew. Chem. Int. Ed.* 56:10282–92
127. Heilbronner E. 1964. Hűckel molecular orbitals of Mőbius-type conformations of annulenes. *Tetrahedron Lett.* 5:1923–28
128. Herges R. 2006. Topology in chemistry: designing Möbius molecules. *Chem. Rev.* 106:4820–42
129. Rzepa HS. 2005. Möbius aromaticity and delocalization. *Chem. Rev.* 105:3697–715
130. Mauksch M, Tsogoeva SB. 2010. Demonstration of "Möbius" aromaticity in planar metallacycles. *Chem. Eur. J.* 16:7843–51
131. Zhu C, Luo M, Zhu Q, Zhu J, Schleyer PVR, et al. 2014. Planar Möbius aromatic pentalenes incorporating 16 and 18 valence electron osmiums. *Nat. Commun.* 5:3265
132. Chen D, Xie Q, Zhu J. 2019. Unconventional aromaticity in organometallics: the power of transition metals. *Acc. Chem. Res.* 52:1449–60
133. Szczepanik DW, Solà M. 2019. Electron delocalization in planar metallacycles: Hückel or Möbius aromatic? *ChemistryOpen* 8:219–227
134. Li W-L, Ivanov AS, Federic J, Romanescu C, Cernusak I, et al. 2013. On the way to the highest coordination number in the planar metal-centred aromatic $Ta©B_{10}^-$ cluster: evolution of the structures of TaB_n^- (n = 3–8). *J. Chem. Phys.* 139:104312
135. Bleeke JR. 2001. Metallabenzenes. *Chem. Rev.* 101:1205–28
136. Fernández I, Frenking G, Merino G. 2015. Aromaticity of metallabenzenes and related compounds. *Chem. Soc. Rev.* 44:6452–63

137. Frogley BJ, Wright LJ. 2018. Recent advances in metallaaromatic chemistry. *Chem. Eur. J.* 24:2025–38
138. Poon KC, Liu L, Guo T, Li J, Sung HHY, et al. 2010. Synthesis and characterization of rhenabenzenes. *Angew. Chem. Int. Ed.* 49:2759–62
139. Chen TT, Li WL, Jian T, Chen X, Li J, Wang L-S. 2017. PrB_7^-: a praseodymium-doped boron cluster with a Pr^{II} center coordinated by a doubly aromatic planar η^7-B_7^{3-} ligand. *Angew. Chem. Int. Ed.* 56:6916–20
140. Li W-L, Chen T-T, Xing D-H, Chen X, Li J, Wang L-S. 2018. Observation of highly stable and symmetric lanthanide octa-boron inverse sandwich complexes. *PNAS* 115:E6972–77
141. Chen T-T, Li W-L, Li J, Wang L-S. 2019. $[La(\eta^x\text{-}B_x)\ La]^-$($x = 7$–9): a new class of inverse sandwich complexes. *Chem. Sci.* 10:2534–42
142. Jiang Z-Y, Chen T-T, Chen W-J, Li W-L, Li J, Wang L-S. 2021. Expanded inverse-sandwich complexes of lanthanum borides: $La_2B_{10}^-$ and $La_2B_{11}^-$. *J. Phys. Chem. A* 125:2622–30
143. Chen T-T, Li W-L, Chen W-J, Li J, Wang L-S. 2019. $La_3B_{14}^-$: an inverse triple-decker lanthanide boron cluster. *Chem. Commun.* 55:7864–67
144. Chen T-T, Li W-L, Chen W-J, Yu X-H, Dong X-R, et al. 2020. Spherical trihedral metalloborospherenes. *Nat. Commun.* 11:2766
145. Cheng S-B, Berkdemir C, Castleman A. 2014. Observation of d–p hybridized aromaticity in lanthanum-doped boron clusters. *Phys. Chem. Chem. Phys.* 16:533–39
146. Cheng S-B, Berkdemir C, Castleman AW. 2015. Mimicking the magnetic properties of rare earth elements using superatoms. *PNAS* 112:4941–45
147. Robinson PJ, Zhang X, McQueen T, Bowen KH, Alexandrova AN. 2017. SmB_6^- cluster anion: covalency involving f orbitals. *J. Phys. Chem. A* 121:1849–54
148. Chen X, Chen T-T, Li W-L, Lu J-B, Zhao L-J, et al. 2019. Lanthanides with unusually low oxidation states in the PrB_3– and PrB_4^- boride clusters. *Inorg. Chem.* 58:411–18
149. Mason JL, Harb H, Huizenga CD, Ewigleben JC, Topolski JE, et al. 2019. Electronic and molecular structures of the CeB_6 monomer. *J. Phys. Chem. A* 123:2040–48
150. Li W-L, Chen T-T, Jiang Z-Y, Wang L-S, Li J. 2020. Recent progresses in the investigation of rare-earth boron inverse sandwich clusters. *Chin. J. Struct. Chem.* 39:1009–18